PAPER

A novel composite of $W_{18}O_{49}$ nanorods on reduced graphene oxide sheets based on *in situ* synthesis and catalytic performance for oxygen reduction reaction†

Jiahao Guo,*[ab] Yantao Shi,*[b] Huawei Zhou,[b] Xuchun Wang[a] and Tingli Ma*[cd]

A novel composite catalyst based on *in situ* synthesis of W_{1+49} nanorods on reduced graphene oxide sheets was successfully fabricated through a one-pot solvothermal route. The as-prepared $W_{18}O_{49}$–reduced graphene oxide (rGO) composite has been systematically characterized by scanning electron microscopy, transmission electron microscopy, X-ray diffraction, Raman microscopy, X-ray photoelectron spectra, and a rotating disk electrode. Compared to $W_{18}O_{49}$ nanorods or reduced graphene oxide alone, or their physical mixture, the composite catalyst exhibited unexpectedly high ORR activity with a more positive onset-potential (close to that of Pt/C) and a higher kinetic current density (J_K), which is mainly attributed to the nanorod morphology, surface oxygen vacancies of $W_{18}O_{49}$, and strong coupling interaction between the $W_{18}O_{49}$ nanorods and reduced graphene oxide sheets. These results raise the possibility of developing low-cost and efficient ORR electrocatalysts.

1. Introduction

Non-precious metal oxides have been actively pursued as catalysts because of their low price, abundance, and environmental compatibility.[1–4] Recently, a wide range of research has been carried out on various metal oxide catalysts such as SnO_2,[5] TiO_2,[6] Fe_3O_4,[7] Co_3O_4,[8] Mn_3O_4–CoO,[9] CoO,[10] $W_{18}O_{49}$.[11] The surfaces of many metal oxides are characterized by a large amount of oxygen vacancies participating in numerous physical and chemical reactions,[12,13] which leads to their important applications in many aspects, including catalysis, electronics, and solar energy technologies.[14] Y. Gorlin and T. Jaramillo proved that the oxygen vacancies in crystalline MnO_x affected its catalytic activity for ORR under alkaline conditions.[15] Dai *et al.* reported that the catalytic activity of Co_3O_4/N-doped graphene hybrid electrocatalysts toward ORR in alkaline media was

sensitive to the number and activity of surface-exposed Co^{3+} ions.[16] Our group also confirmed the presence of abundant oxygen vacancies on the surface of $W_{18}O_{49}$, which were effectively catalyzed the reduction of triiodide (I_3^-) to iodide (I^-), promoted the photoelectric conversion efficiency of dye-sensitized solar cells.[17,18] However, the electrical conductivities of these oxides are poor and restrained its applications in electrocatalysis.[19,20]

Tungsten oxides WO_{3-x} ($x = 0–1$) have been regarded as the most promising candidates for photocatalysts due to their strong adsorption within the solar spectrum.[21,22] Among various tungsten oxides, $W_{18}O_{49}$, one interesting non-stoichiometric tungsten oxide with abundant oxygen vacancies on the surface, is attracting increasing interest because it can be easily fabricated and scaled up, making it suitable for practical applications.[23–25] Ye *et al.* prepared ultrathin $W_{18}O_{49}$ nanowires and applied to the photochemical reduction of CO_2.[26] $W_{18}O_{49}$ nanorods synthesized by Guo *et al.* could effectively adsorb visible light and serve as a photocatalytic material.[27] Zhou *et al.* acquired $W_{18}O_{49}$ with different morphology through controlling the concentration of WCl_6 *via* wet-chemical method.[17,18] Effective combination of metal oxide nanostructures with some conductive carbon materials is believed to be one good strategy to obtain superior electrocatalysts. As a single-layer, two-dimensional sheet of hexagonal carbon, graphene has become a popular catalyst support due to its excellent conductivity, high surface area and good chemical stability. Many graphene-based metal oxide catalysts with outstanding catalytic activities have been reported.[28–30] To date, few research on the controllable

[a]College of Chemistry and Materials Engineering, Anhui Science and Technology University, Fengyang, Anhui, 233100, China. E-mail: tinglima@dlut.edu.cn; guojiahao1974@163.com

[b]State Key Laboratory of Fine Chemicals, School of Chemistry, Dalian University of Technology, Dalian, 116024, China

[c]School Petroleum and Chemical Engineering, Dalian University of Technology, Panjin Campus, Panjin 124221, China

[d]Graduate School of Life Science and Systems Engineering Kyushu Institute of Technology, Kitakyushu, Fukuoka, 808-0196, Japan

assembly of $W_{18}O_{49}$ nanorods supported on reduced graphene oxide (rGO) sheets as ORR electrocatalysts has been reported. Such catalysts are attractive targets, due to the surface oxygen vacancies of $W_{18}O_{49}$ and the conductivity of graphene.

In this work, we demonstrate $W_{18}O_{49}$–rGO composite, which is a novel class of $W_{18}O_{49}$ nanorods supported on reduced graphene oxide sheets synthesized *via* solvothermal method. This *in situ* growth of $W_{18}O_{49}$ on rGO sheets did not disrupt the conductive network of graphene and could significantly decrease the contact resistance between $W_{18}O_{49}$ and rGO. The as-prepared $W_{18}O_{49}$–rGO composite has been systematically characterized. We found the covalent coupling of $W_{18}O_{49}$ nanorods with rGO, suggesting that strongly coupled hybrid materials offer a promising strategy for advanced electrocatalysts. The composite takes an advantage of the activity of $W_{18}O_{49}$ derived from surface oxygen vacancies and the strong coupling with rGO, showing more positive onset potential, higher current density, lower H_2O_2 yield, and greater electron transfer number for ORR in alkaline media than the physical mixture of $W_{18}O_{49}$ nanorods and rGO sheets. Moreover, $W_{18}O_{49}$–rGO possesses a better durability than the commercial Pt/C catalyst.

2. Experimental

2.1 Syntheses of $W_{18}O_{49}$–rGO composite and $W_{18}O_{49}$ nanorod

In a typical procedure for the synthesis of $W_{18}O_{49}$–rGO composite, 1 mg ml^{-1} graphene oxide (GO) ethanol solution was subjected to ultrasonic treatment (950 W, 1 h) and then centrifuged at 4000 rpm for 0.5 h. WCl_6 (60 mg) was dissolved in 48 ml of ethanol to form a clear yellow solution under magnetic stirring, and 12 ml of 1 mg ml^{-1} GO ethanol solution was added to the solution. The mixture was magnetically stirred for 0.5 h, loaded into a Teflon-lined stainless steel autoclave, and heated at 180 °C for 24 h. After cooling to room temperature, the resulting solid product was collected by centrifugation, washed repeatedly with water and ethanol, and vacuum drying at 50 °C overnight.

The synthesis procedure of $W_{18}O_{49}$ nanorod was the same as that for preparing $W_{18}O_{49}$–rGO composite, except that GO ethanol solution was not added during synthesis and the amount of ethanol used was 60 ml.

2.2 Materials characterization

The morphology, structure, and composition of the samples were characterized by different analytic techniques. Scanning electron microscopy (SEM) images were measured with a FEI HITACHI S-4800 field emission scanning electron microscope. Transmission electron microscopy (TEM) images, high-resolution TEM (HRTEM) images, and selected-area electron diffraction (SAED) patterns were taken with a JEOJ-2010 TEM with an acceleration voltage of 200 kV. The X-ray powder diffraction (XRD) profiles were carried out on a Rigaku D/max-rA X-ray diffractometer with Cu Kα radiation (λ = 1.54178 Å). Raman spectra were acquired from a Senterra R200-L Raman

microscope, using a diode laser with excitation at 532 nm. X-ray photoelectron spectra (XPS) were recorded on an ESCALab MKII X-ray photoelectron spectrometer using Mg Kr radiation exciting source.

2.3 Electrochemical tests

Electrochemical measurements were performed at room temperature using a rotating disk working electrode made of glassy carbon (5 mm in diameter) connected to a CHI 660C electrochemical workstation (Chenhua, Shanghai). 4 mg catalyst was redispersed in 1 ml mixed solvents containing deionized water, isopropanol, and Nafion (5%) solution (v/v/v = 2.5 : 1 : 0.06) to form a 4 mg ml^{-1} suspension and ultrasonicated for 1 h to form a homogeneous ink. 5 μL catalyst ink was dropped on the glassy carbon disk electrode, leading to catalyst loading of ∼100 μg cm^{-2} and dried at room temperature. Pt plate and Ag/AgCl (PINE, 4 M KCl) were used as counter and reference electrodes, respectively. The electrochemical experiments were conducted in 0.1 M KOH electrolyte saturated with O_2 at a scan rate of 10 mV s^{-1}. Rotating disk electrode (RDE) measurements were conducted at different rotating speeds from 400 rpm to 2500 rpm. Rotating ring disk electrode (RRDE) measurements were scanned cathodically at a rate of 10 mV s^{-1} with 1600 rpm.

3. Results and discussion

The structure and morphology of the composite materials are examined by SEM and TEM. SEM images of the films on GC electrode with the same amount of $W_{18}O_{49}$–rGO, $W_{18}O_{49}$, rGO, and physical mixture of $W_{18}O_{49}$ and rGO (denoted as mixed $W_{18}O_{49}$ + rGO) are shown in Fig. 1 and S1.† As shown in Fig. 1a and S1a,† the $W_{18}O_{49}$ film consists of 1D nanorods with a length of 100–600 nm and diameter of 15–30 nm. At the end of the nanorods, thick nanorods bundles (NRBs) were formed by short
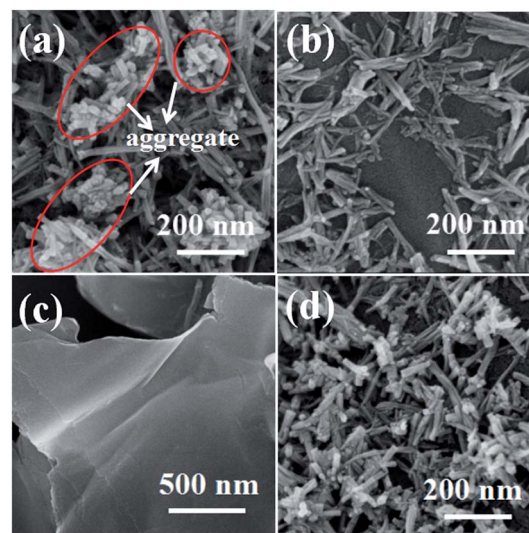

Fig. 1 SEM images of (a) $W_{18}O_{49}$, (b) $W_{18}O_{49}$–rGO, (c) rGO, and (d) mixed $W_{18}O_{49}$ + rGO.

nanorods, indicating an obvious aggregation (red line). Compared with $W_{18}O_{49}$, $W_{18}O_{49}$–rGO sample is composed of nanorods with a few NRBs (Fig. 1b and S1b†). The length of nanorods is between 110–500 nm, which is slightly less than $W_{18}O_{49}$. The diameter of nanorods is equal to $W_{18}O_{49}$, and is about 50 nm for NRBs. Besides few NRBs, no aggregates emerge in $W_{18}O_{49}$–rGO composite, suggesting that the aggregation of $W_{18}O_{49}$ nanorods is effectively reduced by the addition of rGO. The rGO shows a typical sheet structure (Fig. 1c and S1c†). After ultrasonic mixing with $W_{18}O_{49}$ nanorods and rGO, the aggregation degree of $W_{18}O_{49}$ nanorods decreased slightly (Fig. 1d and S1d†).

The TEM images of $W_{18}O_{49}$ (Fig. 2a and S2a†) show that these nanorods ranged from 100 nm to 600 nm with a width of about 20 nm. Cellular aggregation at the end of nanorods is observed, in accord with the SEM results. The HRTEM image shows an inter-planar spacing of 0.39 nm corresponding to the (010) plane of monoclinic $W_{18}O_{49}$ along the [010] direction (Fig. 2b). Among the tungsten oxides, $W_{18}O_{49}$ usually exhibits anisotropic growth along [010], thereby forming 1D nanostructures. This structure is beneficial in forming abundant active sites for oxygen adsorption, which can improve catalytic activity.[31] The SAED pattern of nanorods (Fig. 2c) is consistent with monoclinic $W_{18}O_{49}$. With the existence of GO in solution, $W_{18}O_{49}$ grows along the graphene surface, and $W_{18}O_{49}$ nanorods with diameter of about 20 nm and a size range from 100 nm to 500 nm are obtained on graphene (Fig. 2d and S2b†). The HRTEM image of $W_{18}O_{49}$–rGO in Fig. 2e also displays an inter-planar spacing of 0.39 nm, corresponding to the (010) plane of monoclinic $W_{18}O_{49}$, which is consistent with the SAED pattern Fig. 2f. The growth of $W_{18}O_{49}$ prepared in the absence of GO sheets is similar to those prepared with GO sheets as template, both of which grow along the same direction.[32] This phenomenon commonly occurs in one-dimensional $W_{18}O_{49}$ nanomaterials with monoclinic structure because their close-packed planes are {010}.[33] Fig. 2e also discloses the lattice fringe of connected support with spacing of 0.34 nm, which corresponds well to the (001) plane of graphene.[34] TEM images of graphene and mixed $W_{18}O_{49}$ + rGO are also presented in

Fig. S2† for comparison. The EDX of $W_{18}O_{49}$–rGO composite shows that only C, O, and W can be detected from the TEM grid (Fig. S3†), eliminating other impure elements in the sample.

The XRD patterns in Fig. 3a further confirm the formation of $W_{18}O_{49}$ nanorods and $W_{18}O_{49}$–rGO composite. All diffraction peaks of the XRD pattern of $W_{18}O_{49}$ and $W_{18}O_{49}$–rGO composite are in good agreement with that of monoclinic $W_{18}O_{49}$ (JCPDS 71-2540), proving the successful formation of $W_{18}O_{49}$.[35] In the XRD pattern, two obvious diffraction peaks located approximately at 2θ values of 23.4° and 47.5° can be assigned to the reflection of the (010) and (020) planes, respectively, suggesting that $W_{18}O_{49}$ nanorods preferentially grow along the [010] direction. This result is in accordance with the above HRTEM analysis and SAED patterns. The XRD pattern of $W_{18}O_{49}$–rGO was identical to that of $W_{18}O_{49}$, except for the weak diffraction peak locate at 13.44°, which is associated with the (001) plane of rGO. These results indicates that $W_{18}O_{49}$ successfully grows on graphene sheets by a solvothermal strategy.

The structural features of GO sheets and $W_{18}O_{49}$–rGO composite have been detected using Raman spectroscopy (Fig. 3b). The Raman spectrum of GO displays two strong peaks at 1352 cm^{-1} and 1593 cm^{-1}, which can be assigned to the D band (k-point phonons of A_{1g} symmetry) and the G band (E_{2g} phonon of C sp^2 atoms), respectively.[36] For $W_{18}O_{49}$–rGO composite, the two peaks is obviously shifted to about 1360 cm^{-1} and 1600 cm^{-1} due to the removal of oxygen-containing functional groups following reduction of GO sheets,
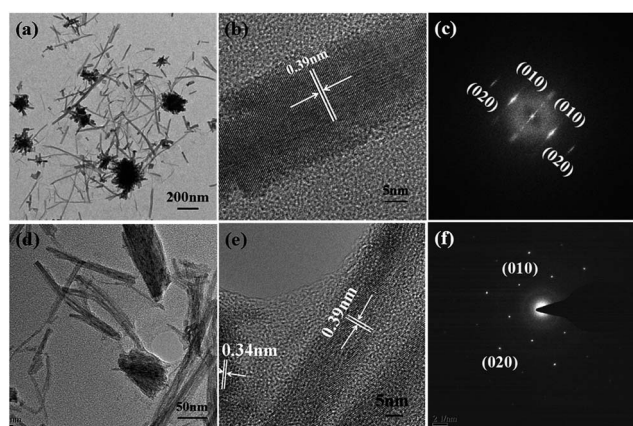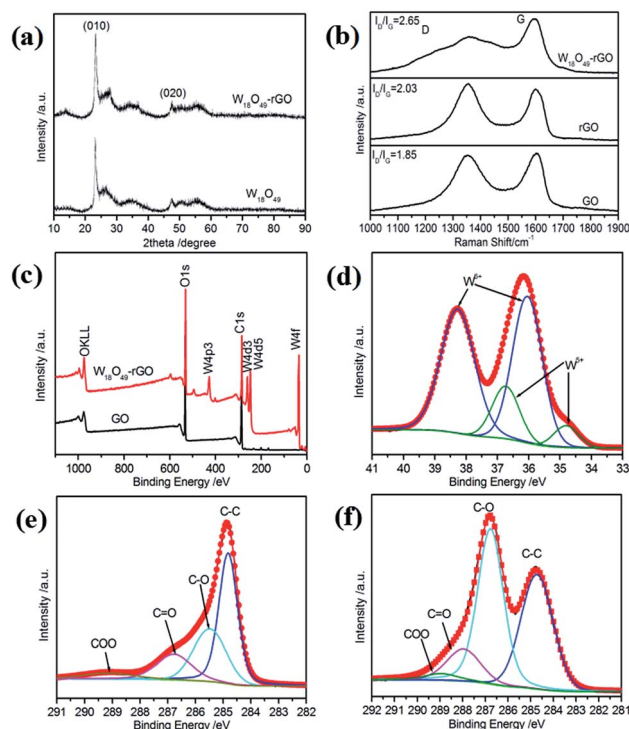

Fig. 3 (a) XRD of $W_{18}O_{49}$–rGO composite catalyst. (b) Raman spectra and (c) XPS spectra of GO and $W_{18}O_{49}$–rGO composite; (d) high-resolution W 4f spectrum and corresponding deconvoluted spectra of $W_{18}O_{49}$–rGO composite; (e) and (f) C 1s core-level and corresponding deconvoluted spectra for $W_{18}O_{49}$–rGO composite and GO.

Fig. 2 TEM, HRTEM, and the corresponding SAED pattern of (a–c) $W_{18}O_{49}$ nanorods and (d–f) $W_{18}O_{49}$–rGO composite.

suggesting an interaction between rGO and $W_{18}O_{49}$ nanorods. This interaction is conducive to promoting the stability of the catalyst interface, endowing the nanocomposites high stability. The Raman spectrum of $W_{18}O_{49}$–rGO also displays that the peak at 250 cm^{-1} can be assigned to the W–O–W bending vibrations and the peaks at 705 and 805 cm^{-1} can be assigned to the W–O–W stretching vibrations (Fig. S5†).[37] Compared with GO, the I_D/I_G values increase from 1.85 to 2.03 for rGO and 2.65 for $W_{18}O_{49}$–rGO composite, suggesting that GO had been reduced after reaction.[38] Furthermore, the I_D/I_G value of $W_{18}O_{49}$–rGO is higher than that of rGO, which indicates the lower overlapping degree of $W_{18}O_{49}$–rGO composite (as graphitic evolution).

The surface elemental composition of GO and $W_{18}O_{49}$–rGO composite is further assessed by XPS. The full-range XPS spectra of GO, rGO, mixed $W_{18}O_{49}$ + rGO, and $W_{18}O_{49}$–rGO composite are shown in Fig. 3c and S7a.† The survey XPS spectra for GO and rGO indicate the presence of oxygen and carbon. However, in the XPS spectra for mixed $W_{18}O_{49}$ + rGO and $W_{18}O_{49}$–rGO composite, tungsten can be detected according to the binding energies. Moreover, no impurities are detected. The deconvolution of the corresponding O 1s spectrum for $W_{18}O_{49}$–rGO composite (Fig. S6†) indicates that at least two chemical bonding states, O 2f and O 3f, are on the surface.[17] The core-level XPS spectrum of W 4f can be deconvoluted into two doublets, which are associated with two different oxidation states of surface W atoms (Fig. 3d and Table 1). The first doublets consists of two peaks with binding energies of 36.1 and 38.4 eV, which belong to W $4f_{7/2}$ and W $4f_{5/2}$ of W^{6+} formal oxidation state, respectively. The second doublet, with lower binding energies of 34.9 and 36.8 eV, is derived from the emission of W $4f_{5/2}$ and W $4f_{7/2}$ core levels from five coordination tungsten atoms, thereby indicating the non-stoichiometric characteristics of the as-synthesized $W_{18}O_{49}$. The emergence of W^{5+} oxidation state shows the presence of oxygen vacancies of $W_{18}O_{49}$ nanorods, which is conducive to the adsorption of oxygen in the catalytic process. Compared with that of mixed $W_{18}O_{49}$ + rGO (Fig. S7b,† Table 1), the W 4f binding energy of W^{6+} of composite are increase from 38.1 eV to 38.4 eV and from 35.9 eV to 36.1 eV. The percentage of W^{5+} for $W_{18}O_{49}$–rGO composite is higher than that for mixed $W_{18}O_{49}$ + rGO, indicating that more oxygen vacancies are present on the surface of $W_{18}O_{49}$–rGO. The core-level XPS spectrum of C 1s and corresponding deconvoluted spectra for GO sheets are shown in Fig. 3e. The peak with binding energy centered at 284.7 eV can

be attributed to the C–C bond. The deconvoluted peaks with binding energies of 286.8, 287.9, and 289.0 eV could be assigned to the C–O, C=O, and COOH bonds, respectively.[39–41] The high-resolution C 1s XPS spectra for $W_{18}O_{49}$–rGO composite shown in Fig. 3f can be fitted with four different components peaks. Compared with GO, $W_{18}O_{49}$–rGO composite shows strong suppression for the oxygen-containing components of their C 1s XPS spectra, suggesting effective reduction of GO sheets *via* the present solvothermal technique. The presence of the binding energy profile at 285.4 eV (C–O bond) indicated a small amount of oxygen-containing carbon groups in the final $W_{18}O_{49}$–rGO composite, which is commonly found in chemically synthesized rGO (Fig. S7d†).[42] Based on the deconvoluted XPS spectra of C 1s peak, the percentages and binding energy of different groups in GO, rGO, mixed $W_{18}O_{49}$ + rGO, and $W_{18}O_{49}$–rGO composite were shown in Table S1.† Compared with GO, after the formation of $W_{18}O_{49}$–rGO composite, the fraction of C–C bond increases from 32.9% to 54.7% and the fraction of C–O bond significantly decreases from 53.2% to 29.3%. Compared with the percentage of C–O of rGO and mixed $W_{18}O_{49}$ + rGO, that of $W_{18}O_{49}$–rGO composite is significantly higher because of the interaction between rGO and $W_{18}O_{49}$. Compared with rGO, the binding energy of different groups in $W_{18}O_{49}$–rGO composite have also increased in different degrees. The increase of W 4f and C 1s binding energy can facilitate the charge transfer between $W_{18}O_{49}$ and rGO. In addition, the C 1s binding energy of $W_{18}O_{49}$–rGO composite is higher compared with those of GO, rGO, and mixed $W_{18}O_{49}$ + rGO (Fig. S8†), indicating a covalent interaction between the rGO sheets and $W_{18}O_{49}$ nanorods.[43] Therefore, a strong effect between $W_{18}O_{49}$ and rGO exists, which is beneficial to the adsorption and charge transfer of oxygen on the catalyst surface.

Based on the above experimental results, the formation of the composite catalyst can be described as follows. First, large GO sheets with abundant oxygen-containing carbon groups on their basal planes and edges are negatively charged when dispersed in ethanol solution.[44] W(VI) centers in the ethanol dissolution of WCl_6 can bind with the oxygen-containing functional groups on GO sheets *via* electrostatic interactions. Upon heating at 180 °C, $W_{18}O_{49}$ nanorods growing along the [010] direction are formed through the hydrolysis of W(VI) centers on the GO sheets under reducing environment. In addition, the growth of $W_{18}O_{49}$ is accompanied with the reduction of GO to rGO during solvothermal process, leading to the formation of $W_{18}O_{49}$–rGO composite.

The ORR electrocatalytic activities of $W_{18}O_{49}$–rGO in O_2-saturated 0.1 M KOH solution have been systematically investigated by cyclic voltammetry (CV), RDE and RRDE methods. Fig. S9† shows the CV curves of different samples in O_2-saturated 0.1 M KOH solutions and all sample loadings are 100 μg cm^{-2}. The ORR peak for $W_{18}O_{49}$–rGO composite is at 0.78 V with a highest current density of 1.36 mA cm^{-2} in all samples, indicating that O_2 can be reduced much more easily on the $W_{18}O_{49}$–rGO composite than other samples.

The RDE linear sweep voltammetry (LSV) curves (Fig. 4a) shows that $W_{18}O_{49}$–rGO composite has an more positive onset potential. The half-wave potential ($E_{1/2}$) of $W_{18}O_{49}$–rGO

Table 1 The XPS fitting results of W 4f for mixed $W_{18}O_{49}$ + rGO and $W_{18}O_{49}$–rGO samples

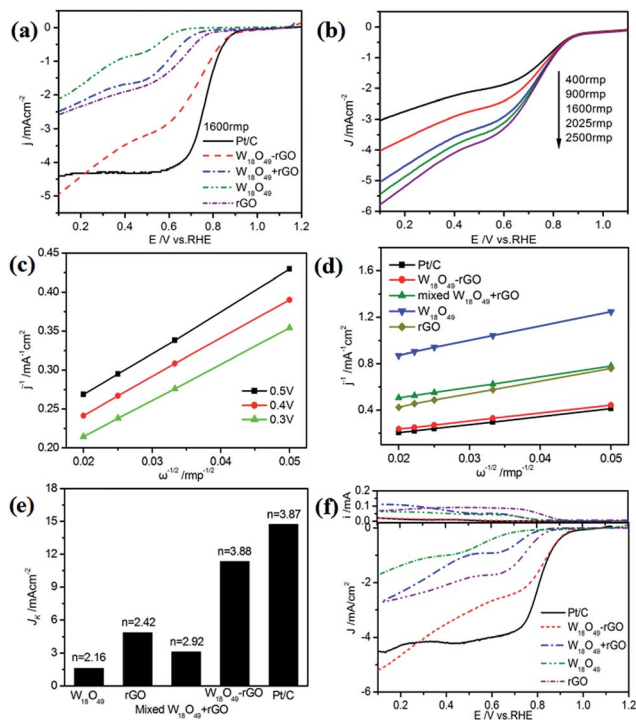| Sample	W 4f	Position (eV)	Percentage
Mixed $W_{18}O_{49}$ + rGO	W^{6+}	38.1	40.1%
		35.9	48.4%
	W^{5+}	34.9	3.5%
		36.8	8.0%
$W_{18}O_{49}$–rGO	W^{6+}	38.4	41.2%
		36.1	40.6%
	W^{5+}	34.9	5.0%
		36.8	13.2%

Fig. 4 (a) LSV of $W_{18}O_{49}$, rGO, mixed $W_{18}O_{49}$ + rGO, $W_{18}O_{49}$–rGO, and Pt/C in O_2-saturated 0.1 M KOH at a scan rate of 10 mV s^{-1} with an RDE rotation rate of 1600 rpm. (b) LSV of $W_{18}O_{49}$–rGO in O_2-saturated 0.1 M KOH at different RDE rotation rates. (c) Calculated K–L plots of ORR from $W_{18}O_{49}$–rGO. (d) K–L plots of ORR from $W_{18}O_{49}$–rGO, $W_{18}O_{49}$ + rGO, $W_{18}O_{49}$, rGO, and Pt/C. (e) Kinetic limiting current density (J_K) and electron transfer number (n) of $W_{18}O_{49}$, rGO, mixed $W_{18}O_{49}$ + rGO, $W_{18}O_{49}$–rGO, and Pt/C. (f) Ring current and disk current compared with Pt/C catalyst (0.80 V). Our results clearly demonstrate that ORR activity of $W_{18}O_{49}$ nanorods in the of $W_{18}O_{49}$, rGO, mixed $W_{18}O_{49}$ + rGO, $W_{18}O_{49}$–rGO, and Pt/C obtained from RRDE measurements.

composite is 0.78 V, which is only 20 mV negative shift composite electrodes is significantly enhanced. The unique combination of $W_{18}O_{49}$ and rGO may play a role in improving the catalytic activity, and the synergetic effect of both components may contribute to enhanced ORR activity of the composite. Accordingly, in combination with the previous characterization, we speculate that $W_{18}O_{49}$ nanorod structures may have potential in providing more active sites for ORR, resulting in enhanced catalytic activity for ORR.

To further explore the ORR behavior, the electron transport number n and kinetic current density J_K have been investigated with RDE based on Koutecky–Levich (K–L) equations:[44,45]

$$\frac{1}{J} = \frac{1}{J_K} + \frac{1}{B\omega^{1/2}} \quad (1)$$

$$B = 0.2nF(D_{O_2})^{2/3}\nu^{-1/6}c_{O_2} \quad (2)$$

where J is the experimental current density, ω is the electrode rotating rate, F is the Faraday constant ($F = 96\,485$ C mol^{-1}), D_{O_2} is the diffusion coefficient of O_2 ($D_{O_2} = 1.9 \times 10^{-5}$ cm s^{-1}). ν is the kinetic viscosity of the electrolyte ($\nu = 0.1$ cm^2 s^{-1}). c_{O_2} is the

bulk concentration of O_2 ($c_{O_2} = 1.2 \times 10^{-6}$ mol cm^{-3}). The constant 0.2 is adopted when the rotation speed is expressed in rpm. The LSV curves of $W_{18}O_{49}$–rGO composite at various rotating speeds are shown in Fig. 4b. The K–L plots calculated from LSVs and compared at 0.4 V at various rotating speeds are shown in Fig. 4c, d and S10.† The electron transport number n of $W_{18}O_{49}$–rGO composite shows the highest value of 3.88 at 0.4 V, similar to ORR catalyzed by commercial Pt/C (3.87), indicating that $W_{18}O_{49}$–rGO catalyst exhibits dominant four-electron oxygen reduction process. J_K value of 11.33 mA cm^{-2} at 0.4 V for $W_{18}O_{49}$–rGO composite is also the largest among our four samples and close to that of Pt/C (14.74 mA cm^{-2}). This result has been suggested to proceed through simultaneous two-oxygen atom side adsorption for oxygen dissociation because of the oxygen vacancies on the surface of $W_{18}O_{49}$.[46] From the Tafel plots as shown in Fig. S11,† $W_{18}O_{49}$–rGO catalyst occupied a much smaller Tafel slope at low over-potential than the other three catalysts, meaning excellent ORR activity. At the same time, we have optimized the ratio of rGO and $W_{18}O_{49}$ in composite catalyst and investigated the effect of catalytic activity for rGO content in composite catalyst (Fig. S12†). It can be seen from the results, the catalytic activity is best when the 12 mg of GO is added. The RRDE measurements shows that the HO_2^- yield of $W_{18}O_{49}$–rGO composite is less than 8%, significantly lower than rGO, $W_{18}O_{49}$ and $W_{18}O_{49}$ + rGO (Fig. 4f and S13†). The electron transfer number is calculated to be ≈ 3.8 over the potential range of 0.1–0.8 V. This is well consistent with the result obtained from the K–L plots based on RDE measurements. Based on these results, we speculate that oxygen molecule is reduced to HO_2^- at $W_{18}O_{49}$ surface and further reduced to OH^- by rGO. Accelerated durability test results show that after 2000 cycles, the half-wave potential of $W_{18}O_{49}$–rGO is negatively shifted by 14 mV, compared to the 15 mV negative shift observed for the Pt/C catalyst (Fig. 5a and b). Chronoamperometric (CA) response results show that $W_{18}O_{49}$–rGO
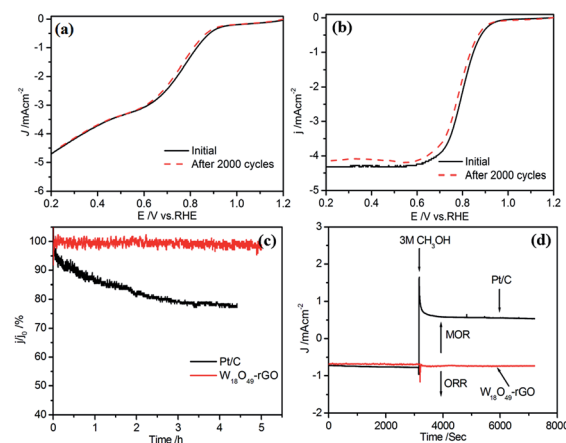

Fig. 5 (a) $W_{18}O_{49}$–rGO and (b) Pt/C before and after 2000 potential cycles in O_2-saturated 0.1 M KOH. The potential was cycled between 0.2 and 1.2 V at a rate of 50 mV s^{-1}. (c) Chronoamperometric response of $W_{18}O_{49}$–rGO and Pt/C. (d) Chronoamperometric response of $W_{18}O_{49}$–rGO and Pt/C before and after addition of 3 M methanol. The tests were conducted in O_2-saturated 0.1 M KOH solution at 0.70 V.

exhibits excellent stability with very slow attenuation for 5 h, with 98.2% of its initial current still persisting (Fig. 5c). This is much better than that of commercial Pt/C catalyst, which lost 23.4% current under the same conditions. The methanol crossover experiment shows that the negative cathodic ORR current of $W_{18}O_{49}$–rGO composite does not show a significant change after the scheduled sequential addition of 3 M methanol into the electrolyte solution, suggesting that its original ORR performance is unaffected by the addition of methanol (Fig. 5d). The excellent long-term stability as well as high selectivity to ORR further suggest that $W_{18}O_{49}$–rGO composite is a very promising ORR electrocatalyst for direct methanol fuel cells.

The excellent ORR performance of this non-precious composite material can be attributed to the nanorod morphology, surface oxygen vacancies of $W_{18}O_{49}$, and strong coupling between metal species and graphene. Specifically, the nanorod morphology can provide numerous surfaces with oxygen vacancies; the oxygen vacancies on the surface of $W_{18}O_{49}$ nanorods are greatly favourable to O_2 adsorption and dissociation. Strong bonding between rGO and $W_{18}O_{49}$ can facilitate electron transfer, which is also a guarantee for the good durability. The (010) facets in $W_{18}O_{49}$ with edge-sharing W–O octahedral are proved to be favorable for catalytic processes because of the high oxidation valence and strong ability to form a redox couple.[47] The prominent ORR catalytic activity of $W_{18}O_{49}$–rGO with (010) facet is probably related to the facile adsorption of oxygen on surface oxygen vacancies of (010) facets of $W_{18}O_{49}$ nanorods during the ORR process. As a result, the $W_{18}O_{49}$–rGO composite with highly exposed (010) facets displays high ORR performance, comparable to the commercial Pt/C.

4. Conclusions

In summary, we have successfully realized the *in situ* growth of $W_{18}O_{49}$ nanorods integrated with rGO sheets to prepare a new $W_{18}O_{49}$–rGO composite catalyst using a simple one-pot solvothermal route. This cheap and facilely prepared non-precious composite electrocatalyst possesses prominent ORR catalytic activity, which is comparable with commercial Pt/C in both reaction current density and onset potential. These advantages can be ascribed to the nanorod morphology, surface oxygen vacancies of $W_{18}O_{49}$, and strong covalent bonding between metal species and graphene. The $W_{18}O_{49}$–rGO composite catalyst also exhibited outstanding fuel crossover resistance and long-term durability in alkaline medium. The *n* value for ORR on the $W_{18}O_{49}$–rGO composite catalyst is 3.88, indicating that the dominant process is the favourable four-electron reduction pathway. This work suggests a great promise for designing effective ORR electrocatalysts by suitable electrical and chemical coupling of cheap functional materials, which is a potentially promising and suitable substitute for the expensive noble metal catalysts in the next generation alkaline and direct methanol fuel cells.

Acknowledgements

Notes and references

1 Y. Y. Liang, Y. G. Li, H. L. Wang, J. G. Zhou, J. Wang, T. Regier and H. J. Dai, *Nat. Mater.*, 2011, **10**, 780.
2 Z. S. Wu, S. Yang, Y. Su, K. Parvez, X. L. Feng and K. Müllen, *J. Am. Chem. Soc.*, 2012, **134**, 9082.
3 Y. F. Xu, M. R. Gao, Y. R. Zheng, J. Jiang and S. H. Yu, *Angew. Chem., Int. Ed.*, 2013, **52**, 8546.
4 M. R. Gao, Y. F. Xu, J. Jiang, Y. R. Zheng and S. H. Yu, *J. Am. Chem. Soc.*, 2012, **134**, 2930.
5 Y. F. Hu, J. Zhou, P. H. Yeh, Z. Li, T. Y. Wei and Z. L. Wang, *Adv. Mater.*, 2010, **22**, 3327.
6 K. Nakata and A. Fujishima, *J. Photochem. Photobiol., C*, 2012, **13**, 169.
7 Y. X. Ye, L. Kuai and B. Y. Geng, *J. Mater. Chem.*, 2012, **22**, 19132.
8 R. Jing, A. X. Shan, R. M. Wang and C. P. Chen, *CrystEngComm*, 2013, **15**, 3597.
9 J. W. Xiao, L. Wan, X. Wang, Q. Kuang, S. Dong, F. Xiao and S. Wang, *J. Mater. Chem. A*, 2014, **2**, 3794.
10 H. T. Yu, Y. C. Li, X. H. Li, L. Z. Fan and S. H. Yang, *Chem.–Eur. J.*, 2014, **20**, 3457.
11 H. W. Zhou, Y. T. Shi, L. Wang, H. Zhang, C. Y. Zhao, A. Hagfeldt and T. L. Ma, *Chem. Commun.*, 2013, **49**, 7626.
12 R. Schaub, E. Wahlstrom, A. Ronnau, E. Laegsgaard, I. Stensgaard and F. Besenbacher, *Science*, 2003, **299**, 377.
13 D. Matthey, J. G. Wang, S. Wendt, J. Matthiesen, R. Schaub, E. Lægsgaard, B. Hammer and F. Besenbacher, *Science*, 2007, **315**, 1692.
14 H. Over, *Chem. Rev.*, 2012, **112**, 3356.
15 Y. Gorlin and T. Jaramillo, *J. Am. Chem. Soc.*, 2010, **132**, 13612.
16 Y. Y. Liang, Y. G. Li, H. L. Wang, J. G. Zhou, J. Wang, T. Regier and H. J. Dai, *Nat. Mater.*, 2011, **10**, 780.
17 H. W. Zhou, Y. T. Shi, L. Wang, H. Zhang, C. Y. Zhao, A. Hagfeldt and T. L. Ma, *Chem. Commun.*, 2013, **49**, 7626.
18 H. W. Zhou, Y. T. Shi, Q. S. Dong, Y. X. Wang, C. Zhu, L. Wang, N. Wang, Y. Wei, S. Y. Tao and T. L. Ma, *J. Mater. Chem. A*, 2014, **2**, 4347.
19 G. Q. Zhang, B. Y. Xia, X. Wang and X. W. Lou, *Adv. Mater.*, 2014, **26**, 2408.
20 Y. Y. Liang, H. L. Wang, P. Diao, W. Chang, G. S. Hong, Y. G. Li, M. Gong, L. M. Xie, J. G. Zhou, J. Wang, T. Z. Regier, F. Wei and H. J. Dai, *J. Am. Chem. Soc.*, 2012, **134**, 15849.
21 X. H. Zhang, X. H. Lu, Y. Q. Chen, J. B. Han, L. Y. Yuan, L. Gong, Z. Xu, X. D. Bai, M. Wei, Y. X. Tong, Y. H. Gao,

J. Chen, J. Zhou and Z. L. Wang, *Chem. Commun.*, 2011, **47**, 5804.

22 Z. G. Zhao, Z. F. Liu and M. Miyauchi, *Chem. Commun.*, 2010, **46**, 3321.

23 C. S. Guo, S. Yin, Q. Dong and T. Sato, *RSC Adv.*, 2012, **2**, 5041.

24 S. B. Sun, Y. M. Zhao, Y. D. Xia, Z. D. Zou, G. H. Min and Y. Q. Zhu, *Nanotechnology*, 2008, **19**, 305.

25 D. Wang, J. Li, X. Cao, G. S. Peng and S. H. Feng, *Chem. Commun.*, 2010, **46**, 7718.

26 G. Xi, S. Ouyang, P. Li, J. Ye, Q. Ma, N. Su, H. Bai and C. Wang, *Angew. Chem., Int. Ed.*, 2012, **51**, 2395.

27 C. Guo, S. Yin, M. Yan, M. Kobayashi, M. Kukihana and T. Sato, *Inorg. Chem.*, 2012, **51**, 4763.

28 J. T. Zhang, C. X. Guo, L. Y. Zhang and C. M. Li, *Chem. Commun.*, 2013, **49**, 6334.

29 Z. S. Wu, S. B. Yang, Y. Sun, K. Parvez, X. L. Feng and K. Mullen, *J. Am. Chem. Soc.*, 2012, **134**, 9082.

30 Y. Y. Liang, H. L. Wang, P. Diao, W. Chang, G. S. Hong, Y. G. Li, M. Gong, L. M. Xie, J. G. Zhou, J. Wang, T. Z. Regier, F. Wei and H. J. Dai, *J. Am. Chem. Soc.*, 2012, **134**, 15849.

31 J. Lee, G. Park, H. Lee, S. Kim, R. Cao, M. Liu and J. Cho, *Nano Lett.*, 2011, **11**, 5362.

32 X. T. Chang, L. H. Dong, Y. S. Yin and S. B. Sun, *RSC Adv.*, 2013, **3**, 15005.

33 Y. Z. Jin, Y. Q. Zhu, R. L. D. Whitby, N. Yao, R. Z. Ma, P. C. P. Watts, H. W. Kroto and D. R. M. Walton, *J. Phys. Chem. B*, 2004, **108**, 15572.

34 T. F. Yeh, J. M. Syu, C. Cheng, T. H. Chang and H. S. Teng, *Adv. Funct. Mater.*, 2010, **20**, 2255.

35 H. W. Zhou, Y. T. Shi, Q. S. Dong, Y. X. Wang, C. Zhu, L. Wang, N. Wang, Y. Wei, S. Y. Tao and T. L. Ma, *J. Mater. Chem. A*, 2014, **2**, 4347.

36 H. J. Song, X. H. Jia, N. Li, X. F. Yang and H. Tang, *J. Mater. Chem.*, 2012, **22**, 895.

37 F. Xu, A. Fahmi, Y. M. Zhao, Y. D. Xia and Y. Q. Zhu, *Nanoscale*, 2012, **4**, 7031.

38 X. G. Bai, Y. T. Shi, H. J. Guo, L. G. Gao, K. Wang, Y. Du and T. L. Ma, *J. Power Sources*, 2016, **306**, 85–91.

39 J. P. Zhao, S. F. Pei, W. C. Ren, L. B. Gao and H. M. Cheng, *ACS Nano*, 2010, **4**, 5245.

40 H. X. Tang, G. J. Ehlert, Y. R. Lin and H. A. Sodano, *Nano Lett.*, 2012, **12**, 84.

41 Z. X. Jiang, J. J. Wang, L. H. Meng, Y. D. Huang and L. Liu, *Chem. Commun.*, 2011, **47**, 6350.

42 S. Stankovich, D. A. Dikin, R. D. Piner, K. A. Kohlhaas, A. Kleinhammes, Y. Jia, Y. Wu, S. T. Nguyen and R. S. Ruoff, *Carbon*, 2007, **45**, 1558.

43 D. Joung, V. Singh, S. Park, A. Schulte, S. Seal and S. I. Khondaker, *J. Phys. Chem. C*, 2011, **115**, 24494.

44 S. Wang, D. Yu and L. Dai, *J. Am. Chem. Soc.*, 2011, **133**, 5182.

45 L. Y. Zhang, C. X. Guo, Z. Cui, J. Guo, Z. Dong and C. M. Li, *Chem.–Eur. J.*, 2012, **18**, 15693.

46 S. Kattel, P. Atanassov and B. Kiefer, *Phys. Chem. Chem. Phys.*, 2013, **15**, 148.

47 H. Huang, Q. Yu, X. Peng and Z. Ye, *Chem. Commun.*, 2011, **47**, 12831.